Journal of Nuclear Materials 300 (2002) 178–191

journal of nuclear materials

www.elsevier.com/locate/jnucmat

Influence of dynamic strain aging on the ductile tearing of C–Mn steels: modelling by a local approach method

D. Wagner [a,*], J.C. Moreno [a], C. Prioul [a], J.M. Frund [b], B. Houssin [c]

[a] *Laboratoire MSS/MAT CNRS UMR 8579, Ecole Centrale de Paris, Grande voie des vignes, 92295 Chatenay Malabry cedex, France*
[b] *E.D.F., Division Recherche et Développement, France*
[c] *Framatome, Département Matériaux et Technologie, France*

Received 5 March 2001; accepted 6 November 2001

Abstract

C–Mn steels and associated welds can be susceptible to dynamic strain aging (DSA). In this case, fracture toughness passes through a minimum when the temperature increases from 20 to 300 °C. Since Charpy V-Notch data are not affected by the DSA phenomenon, the method for predicting the evolution of $J_{0.2}$ and $\mathrm{d}J/\mathrm{d}a$ in the temperature domain where DSA occurs is still an open question. The purpose of the present study is the assessment of this decrease in fracture toughness using a local approach method. The results of J–R tearing resistance tests, characterized by crack initiation resistance $J_{0.2}$ and tearing modulus $\mathrm{d}J/\mathrm{d}a$ relative to a base metal (A48 French standard steel) and manual metal arc deposited metals are presented and discussed. The local approach determination of $J_{0.2}$ was performed using the Rice and Tracey model. Comparisons between experimental results and the results of local approach modelling indicate that both $J_{0.2}$ and $\mathrm{d}J/\mathrm{d}a$ decreases with DSA can be correctly predicted. © 2002 Published by Elsevier Science B.V.

1. Introduction

Pipes, plates and associated welds in carbon–manganese steels, are commonly used for the secondary systems (feedwater line and steam line) of pressurized water reactors. These steels are well known to be sensitive to dynamic strain aging (DSA) when insufficiently killed. This phenomenon, which is observed in metals containing solute atoms such as nitrogen that interact with dislocations [1–6], induces an increase in flow stress, ultimate tensile strength (UTS) and work hardening rate, as well as a decrease in ductility (elongation, reduction of area, strain rate sensitivity coefficient and fracture toughness). DSA can produce various types of inhomogeneous deformations known as the Portevin–Le-Chatelier (PLC) effect [6]. It is observed in a temperature range which is clearly dependent on the mobility of the solute atoms relative to the imposed dislocation velocity [7–12].

In C–Mn steels, it is well established [1] that the diffusing solute species are interstitial carbon and nitrogen atoms. Moreover, due to its greater solubility limit [5,13], nitrogen content seems to exert a more pronounced influence on strain aging than carbon content. Depending on the diffusion coefficients, the chemical composition of the steels and the strain rate, DSA occurs in the temperature range 200–350 °C.

A literature review [13–20] shows that in commercial C–Mn steels sensitive to DSA (base metals and deposited metals) and at normal strain rate tests, the fracture toughness (crack initiation resistance $J_{0.2}$ or J_{Ic} and tearing modulus $\mathrm{d}J/\mathrm{d}a$) decreases from room temperature to about 200 °C, and then increases for higher temperatures. This behaviour is also observed in low alloy steels sensitive to DSA [21–23].

---

[*] Corresponding author. Tel.: +33-1 4113 1239; fax: +33-1 4113 1430.
E-mail address: wagner@mssmat.ecp.fr (D. Wagner).

0022-3115/02/$ - see front matter
PII: S0022-3115(01)00746-2

This detrimental effect of DSA on ductile tearing resistance does not occur in all iron base materials. Srinivas et al. [23,24] and Hong and Linga Murty [25] show the opposite behaviour in pure armco iron, i.e. the fracture toughness (crack initiation resistance and tearing modulus) increases from room temperature to 200 °C and then decreases. However, this material shows the same DSA effect as other materials on tensile properties (i.e. a maximum in UTS and work hardening rate, a minimum in elongation and reduction of area). This different behaviour is attributed to the absence of inclusions in pure iron which modifies the ductile damage mechanism.

In commercial C–Mn or low alloy steels and associated welds, the ductile damage mechanism is mainly governed by second phases particles or manganese sulphide or oxide inclusions. Three principal stages in the damage mechanism have been recently reviewed by Thomason [26]. The first stage (I) is the nucleation of microvoids on second phase particles or inclusions. This occurs when the plastic deformation of the matrix has raised the matrix/particle interface stress up to the level where particles either crack or disbond from the matrix. The second stage (II) consists of the growth of microvoids under the applied plastic stress and strain rate field up to the point where the intervoid matrix reaches its loading capacity limit. The third stage (III) corresponds to the plastic limit-load failure of the intervoid matrix when a catastrophic process of internal microscopic necking causes localized plastic failure and separation of the intervoid matrix material.

At room temperature, the fracture toughness of C–Mn steels is essentially governed by the volume fraction of MnS inclusions (base metal) or oxides (deposited metal) [27–31]. In this case, fracture toughness can be estimated from Charpy V-Notch tests through various correlations [32].

When the temperature increases, the upper shelf level Charpy V-Notch data remain unchanged and are not affected by the DSA phenomenon. This is due to the high strain rate of Charpy V-Notch tests. Thus, the decrease of $J_{0.2}$ and $\mathrm{d}J/\mathrm{d}a$ with temperature due to DSA cannot be predicted from Charpy V-Notch data. However, a correlation has been established previously (Fig. 1, [14]) between the decrease of $J_{0.2}$ ($J_{0.2}^{20\ °\mathrm{C}} - J_{0.2}^{\mathrm{min}}/J_{0.2}^{20\ °\mathrm{C}}$) and the increase of UTS ($\mathrm{UTS}^{\mathrm{max}} - \mathrm{UTS}^{20\ °\mathrm{C}}/\mathrm{UTS}^{20\ °\mathrm{C}}$); the greater the sensitivity to DSA measured by tensile tests, the greater the decrease of $J_{0.2}$.

Furthermore, the temperatures at the minima in $J_{0.2}$ and $\mathrm{d}J/\mathrm{d}a$ depend on both strain rate and chemical composition (in the same way as the temperature of the maximum in UTS and work hardening rate). When strain rate increases, the temperature of the minima increases [18,22] according to the thermally activated phenomenon involved in DSA. As regards the influence of chemical composition, manganese is the main element that modifies this temperature. An increase in manganese content increases the maximum temperature for the UTS [33]. This effect, which is still not clearly identified, could be due to an interaction between manganese and nitrogen (and carbon). For deposited materials with high manganese content, the $J_{0.2}$ and $\mathrm{d}J/\mathrm{d}a$ minima would then be located at temperatures higher than 200 °C.

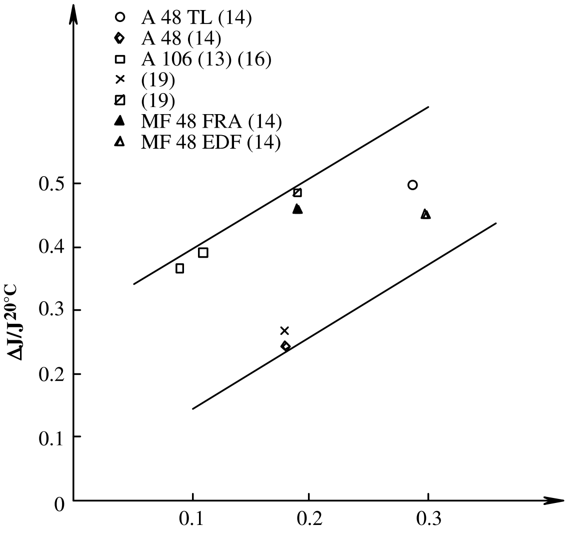

Fig. 1. Correlation between DSA sensitivity measured by tensile tests and decrease of crack initiation resistance $J_{0.2}$.

Taking into account the above mentioned phenomena, the prediction from tensile tests results of the evolution of $J_{0.2}$ and $\mathrm{d}J/\mathrm{d}a$ in the temperature domain where DSA occurs is still an open question. Therefore the objective of the present study is the assessment of this decrease using a local approach method for ductile fracture.

Two materials were tested: one base metal, A48 (French standard), and one a weld metal deposited by manual metal arc welding (MMAW). The damage model used is the Rice and Tracey model for cavity growth [34]. The $J_{0.2}$ value at ductile tearing initiation is related to the calculated value of void growth at failure $(R/R_0)_c$, where R_0 is the initial radius of the manganese sulphides inclusions and R is the failure radius of the cavity nucleated from this inclusions. The parameter $(R/R_0)_c$ can be determined from experiments conducted on axisymmetric notched specimens tested to failure, and finite element calculations of the stress and strain fields in such specimens.

Failure was characterized by tensile tests performed in the 20–300 °C temperature range on axisymmetric notched specimens, as well as by tearing resistance (J–R) tests. Predicted $J_{0.2}$ values were then compared to experimental $J_{0.2}$ values.

2. Materials and experimental procedure

2.1. Materials

Two materials were investigated in this study. First, a wrought base metal to the AFNOR (French Standard) NFA 36205 grade A48 which was received as a 40 mm thick plate. The chemical composition is given in Table 1. This material is a silicon semi-killed steel containing a very low aluminium content. The later element is usually present in insufficient amounts to be capable of trapping nitrogen atoms as aluminium nitride (AlN) during cooling from the austenitic domain. Consequently, a large amount of free nitrogen is still present in the lattice making this alloy sensitive to DSA. The plate received a prior normalization thermal treatment consisting of austenitizing at 870 °C, then air cooling, leading to a microstructure composed of banded ferrite and pearlite.

The distribution of inclusions was characterized on polished sections perpendicular to the three principal directions relative to the rolling direction (longitudinal, L, transverse, T and short transverse, S). Two populations were observed: small spherical particles and clusters of large mixed inclusions. A semi-quantitative chemical analysis made using the EDS technique showed that small inclusions were manganese sulphide (MnS) particles and the large ones were mixed silicon and aluminium oxides (Al_2O_3, SiO_2, CaO) as well as manganese sulphides. The inclusion volume fraction f_V was estimated from the chemical composition using Franklin's formula [35]:

$$f_V = 0.054\left(\%S - \frac{0.0014}{\%Mn}\right) + 0.05\ \%O = 0.079\%. \qquad (1)$$

The second material was a weld metal deposited by multipass MMAW using a basic coated electrode (SAFER MF48). The chemical analysis is given in Table 2.

Table 1
A48 steel chemical composition (wt%)

C	0.198
S	0.012
P	0.0104
Si	0.207
Mn	0.769
Ni	0.135
Cr	0.095
Mo	0.025
V	<0.003
Cu	0.273
Sn	0.023
Al	0.004
N	0.0083
O	0.0049
Ti	<0.003
Nb	<0.004

Table 2
MMAW weld metal chemical composition (wt%)

C	0.049
S	0.007
P	0.018
Si	0.4
Mn	0.86
Ni	0.043
Cr	0.021
Mo	0.008
V	0.023
Cu	0.016
Sn	0.005
Al	<0.005
N	0.012
O	0.038
Ti	0.009
Nb	0.005

In as-deposited metals, the small amount of aluminium (<0.005%) is trapped by oxygen (which is still present in high concentration compared to base metal) as aluminium oxides Al_2O_3. In this case, the remaining aluminium content is not sufficient to allow the precipitation of aluminium nitride (AlN) for trapping nitrogen, thus explaining the significant sensitivity of deposited weld metals to DSA. For this electrode type, the manganese content is of the same order as that of the base metal (about 0.8%).

In a multipass weld, each successive pass induces reheating of the layer below. The recrystallized affected zone observed by optical microscopy consisted of both fine grained and coarse grained ferrite. In each weld bead layer, a non-recrystallized zone was still present which contained proeutectoid ferrite, lamellar bainite and acicular ferrite.

A semi-quantitative chemical analysis was also performed on the MMAW weld metal. This analysis showed spherical mixed inclusions of manganese sulphide (MnS), titanium oxide (TiO_2) and mainly manganese–silicon oxide ($2MnO–SiO_2$). The inclusion volume fraction f_V was estimated from the chemical composition using the following formula [36]:

$$f_V = 0.053\%S + 0.0367\%Ti + 0.064\%O = 0.31\%. \qquad (2)$$

2.2. Experimental procedure

2.2.1. Tensile tests

Smooth specimens: Tensile tests on smooth specimens were performed in the temperature range 20–300 °C at a strain rate of $2 \times 10^{-4}\ s^{-1}$. The experimental details and results were presented in a previous paper [14]. In the temperature range of interest, both materials display a maximum UTS and work hardening rate at 200 °C as well as a ductility minimum (located at about 150 °C for the elongation and strain rate sensitivity and at 200 °C for the reduction of area). Both materials appeared to be sensitive to DSA.

Axisymmetric notched specimens: In order to determine the influence of stress triaxiality on ductility and to calculate the critical void growth parameter $(R/R_0)_c$, tests on axisymmetric notched specimens (shown in Fig. 2) were performed over the same temperature range at a nominal strain rate of 10^{-4} s^{-1} (nominal strain rate being defined as the mean value of the strain rate in the minimum cross-section). The initial diameter Φ_0 under the notch was 10 mm for all samples, but the root notch radius *r* varied from 2 mm (AE2), 4 mm (AE4) and up to 10 mm (AE10). The specimen locations in the weldment were given in Fig. 3.

During the tensile tests, the load *P* versus diameter Φ, measured at the minimum section were recorded. From these values, the mean stress $\bar{\sigma} = 4P/\pi\Phi_0^2$ and the mean strain $\bar{\varepsilon} = 2\ln(\Phi_0/\Phi)$ were calculated. The mean stress and strain at failure (σ_R and ε_R respectively) were determined (ε_R from final diameter Φ_R measured on broken specimens).

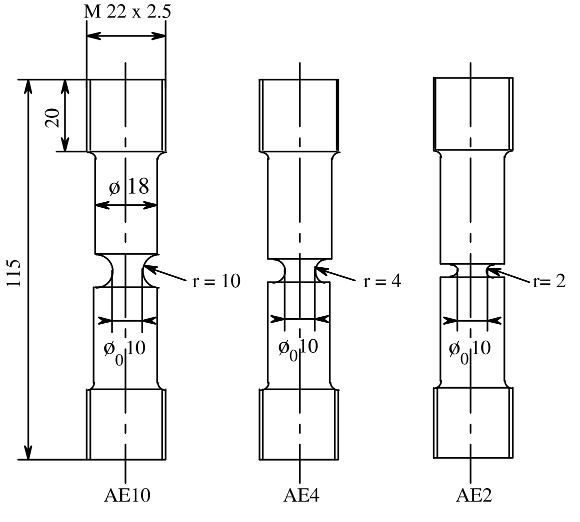

Fig. 2. Axisymmetric notched specimens (all dimensions are in mm).

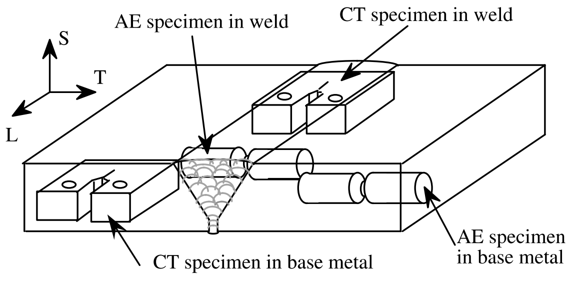

Fig. 3. Location of specimens in weldment.

2.2.2. Tearing resistance tests (J–R tests)

J–R tests were performed on 20% side-grooved CTJ 25 specimens for the base metal and side-grooved CTJ 20 for the weld deposited metal taken as indicated in Fig. 3. The temperature range of the tests was 20–300 °C for the base metal and 100–300 °C for the weld deposited metal. The test rate was taken between 1×10^{-2} and 3×10^{-3} mm/min. A simplified calculation has shown that in this case, the strain rate at the notch root is about 5×10^{-4} s^{-1} at 20 °C, i.e., equivalent to the applied strain rate in axisymmetric specimens.

The general experimental procedure used was the partial unloading compliance method (except for one test at 300 °C for the deposited metal, where the multispecimen method was used). The tests were analyzed by the GFR single specimen test procedure [37] taking into account a simple rotation correction, without zero point correction for the base metal but with zero point correction for the weld deposited metal. Conventional crack initiation and propagation values were computed from the data: $J_{0.2}$ (*J* value for 0.2 mm crack propagation) and d*J*/d*a*.

3. Experimental results

3.1. Tensile tests on axisymmetric notched specimens

For the two materials, the PLC effect is observed as serrations on the mean stress versus mean strain curves $(\bar{\sigma}, \bar{\varepsilon})$ between 100 and 200 °C, independent of the geometry of the specimens (Fig. 4). The variations of the mean strain at failure ε_R for smooth specimens and axisymmetric specimens with different notch radii are

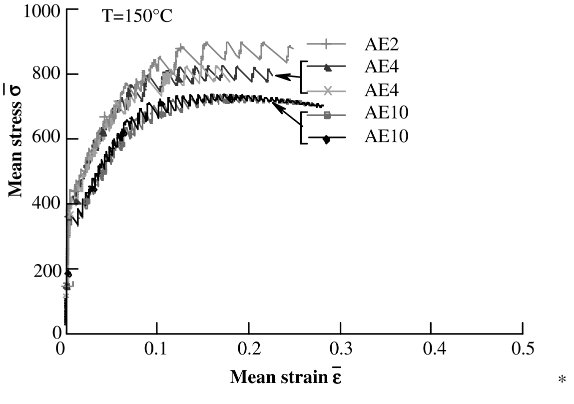

Fig. 4. Variation of mean stress versus mean strain at 150 °C for the base metal.

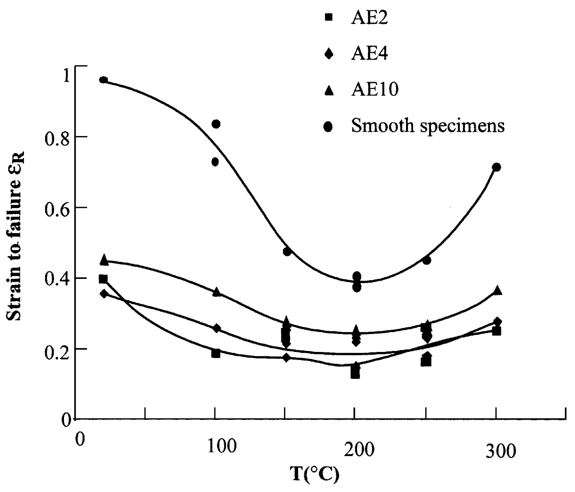

Fig. 5. Variation of strain to failure versus temperature for different specimen geometries (base metal).

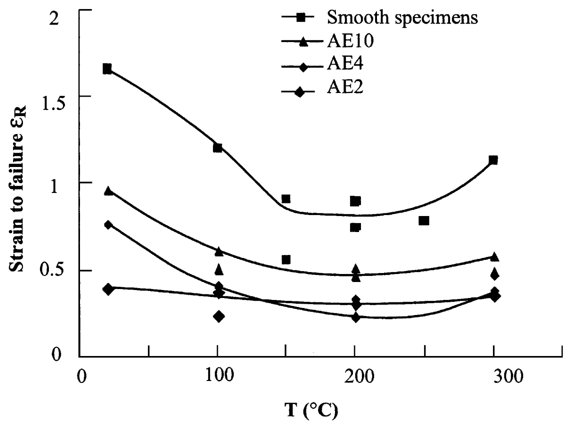

Fig. 6. Variation of strain to failure versus temperature for different specimen geometries (weld deposited metal).

plotted versus temperature in Fig. 5 for the base metal and Fig. 6 for the weld deposited metal. The strain value at failure is calculated from the reduction of area Z using the following relation $\varepsilon_R = \ln(1/1 - Z)$. A ductility trough is located near 200 °C independent of specimen geometry. The increase in triaxiality with decreasing notch radius, induced a decrease in mean strain to failure at all temperatures.

3.2. Tearing resistance tests (J–R tests)

The experimental compliance load–displacement curves also show serrations (PLC effect) at 200 °C (Fig. 7(a)). Moreover, as reported previously by Miglin et al. [16], due to the unloading procedure used, a static strain aging phenomenon occurs, especially at 100 °C (Fig. 7(b)). This effect is revealed clearly by the appearance of transient overload peaks on the reloading curves.

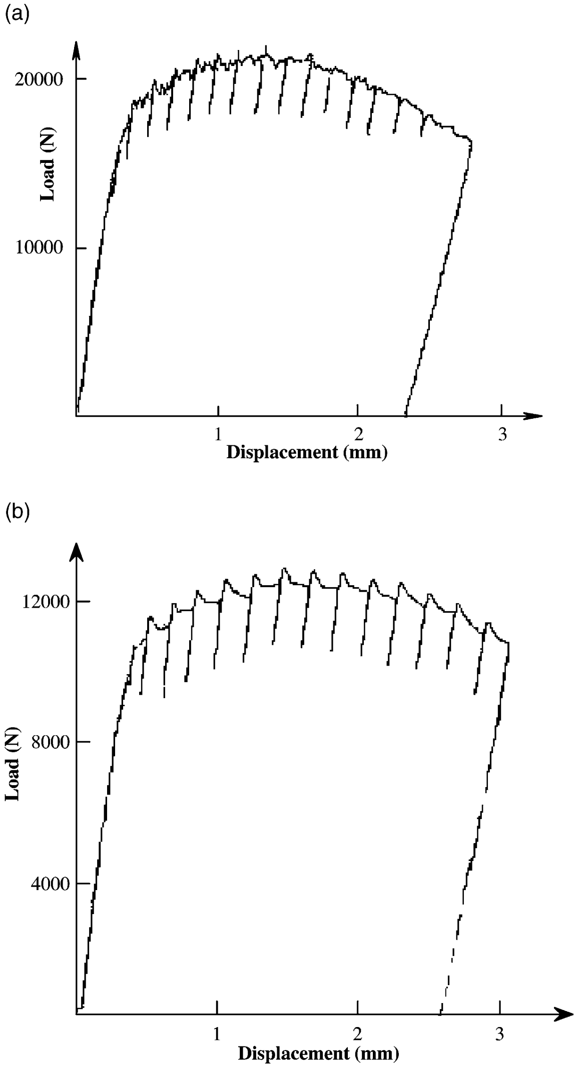

Fig. 7. Load–displacement curves at $T = 200$ °C (a) and $T = 100$ °C (b) for the base metal.

The variations of crack initiation resistance $J_{0.2}$ and tearing modulus $\mathrm{d}J/\mathrm{d}a$ are plotted versus temperature in Figs. 8 and 9. As reported in the literature for commercial steels, these two characteristics pass through a sharp minimum in the temperature range tested (20 or 100–300 °C).

4. Modelling

In this study, the damage model proposed by Rice and Tracey [35] was used. The damage process is controlled by the growth of voids initiated at inclusions. The

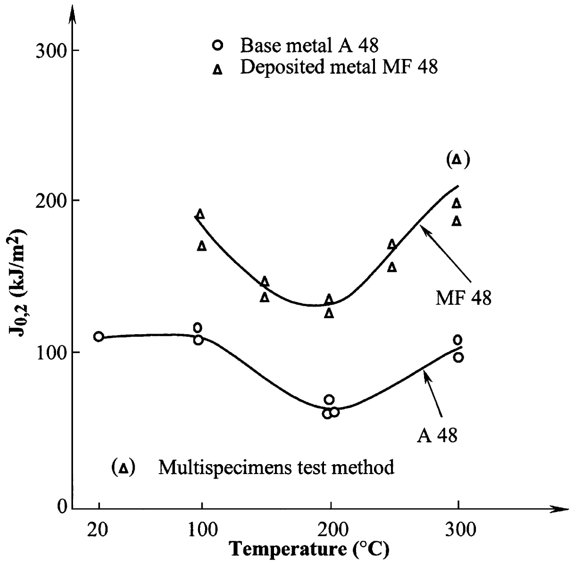

Fig. 8. Variation of crack initiation resistance $J_{0.2}$ versus temperature for the base and weld deposited metals.

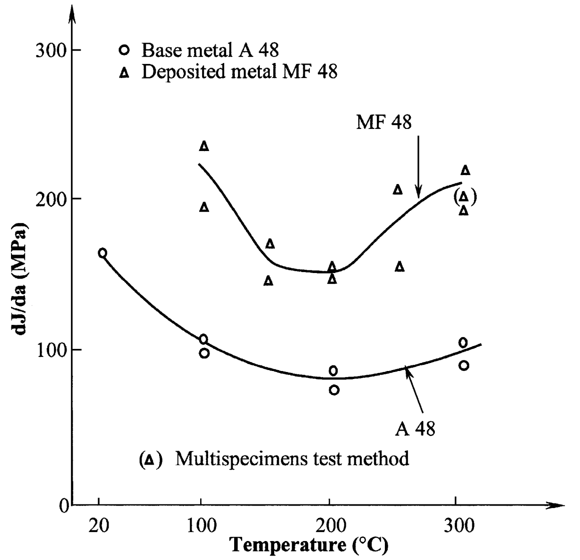

Fig. 9. Variation of the tearing modulus $\mathrm{d}J/\mathrm{d}a$ versus temperature for base and weld deposited metals.

evolution of void growth rate versus equivalent stress and strain, and mean strain is given by

$$\frac{\dot{R}}{R} = \dot{\varepsilon}^{\mathrm{p}}_{\mathrm{eq}} 0.283 \exp\left(\frac{3}{2}\frac{\sigma_{\mathrm{m}}}{\sigma_{\mathrm{eq}}}\right), \tag{3}$$

where R is the actual cavity radius; $\dot{R}$ is the cavity growth rate; $\dot{\varepsilon}^{\mathrm{p}}_{\mathrm{eq}}$ is the equivalent plastic strain rate; σ_{m} is the hydrostatic stress; σ_{eq} is the Von Mises equivalent stress.

This model was established assuming a rigid plastic matrix. Beremin [38] showed that it is also possible to use the model made for high strain hardening materials, as in the present case. The flow stress is then substituted by the Von Mises equivalent stress.

The third stage of final failure of the intervoid matrix cannot be modelled by the Rice and Tracey model. Thus, failure is assumed to occur at a critical value of void growth $(R/R_0)_{\mathrm{c}}$. This parameter is calculated by integrating the Rice and Tracey expression between ε_{d} (strain necessary to nucleate cavities from inclusions) and ε_{R} (strain at failure).

$$\ln\left(\frac{R}{R_0}\right)_{\mathrm{c}} = \int_{\mathrm{nucleation}}^{\mathrm{failure}} f\left(\frac{\sigma_{\mathrm{m}}}{\sigma_{\mathrm{eq}}}\right) \mathrm{d}\varepsilon_{\mathrm{eq}}. \tag{4}$$

To apply this model, knowledge of the stress and strain fields in the notched axisymmetric tensile specimens is therefore necessary.

4.1. Numerical procedure

The numerical analysis of the three geometries of axisymmetric notched specimens using the finite element method under large scale yielding was conducted using the ABAQUS 5.4 software. The mesh is shown in Fig. 10. The elements are eight node quadratic elements (with reduced integration). The applied boundary conditions were the following: symmetry, displacement equal to zero on the axis of symmetry in direction 1 (Fig. 10), displacement equal to zero on the minimum section in direction 2 (Fig. 10), and fixed displacement at the specimen head in direction 2. The minimum section was divided into 15 elements, whose characteristic dimension was 0.33 mm.

The constitutive equations of the material took into account both elastic and plastic isotropic behaviour with

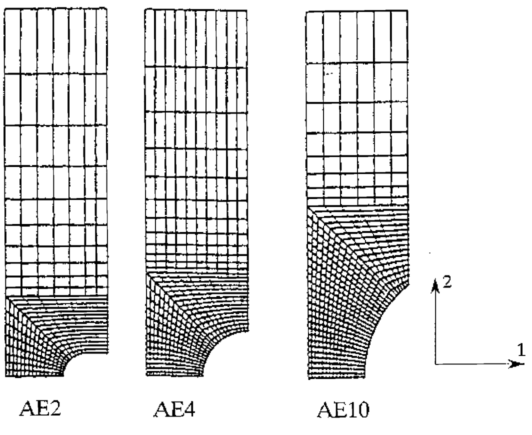

Fig. 10. Mesh geometries for finite element calculations.

non-linear work hardening. They were determined from tensile tests on smooth specimens [14] and are shown in Fig. 11(a) and (b) for the A48 base metal. They were introduced into the calculations using a point-by-point procedure. Due to the high work hardening rate in the DSA temperature range, a detailed description of the curves is needed (Fig. 11(b)). The predicted variations of the mean stress $\bar{\sigma}$ versus the mean strain $\bar{\varepsilon}$ calculated from the numerical analysis are shown in Fig. 12 for the A48 base metal at a temperature of 150 °C. For comparison purposes, the experimentally measured variations are also shown in this figure. The numerical modelling is considered to be satisfactory, when the difference between the calculated and experimental results is less than 5%. For the curves with serrations (in the PLC temperature range), the calculated curve is fitted to the upper part of the serrations since negative strain rate sensitivity cannot be easily included in the constitutive equations.

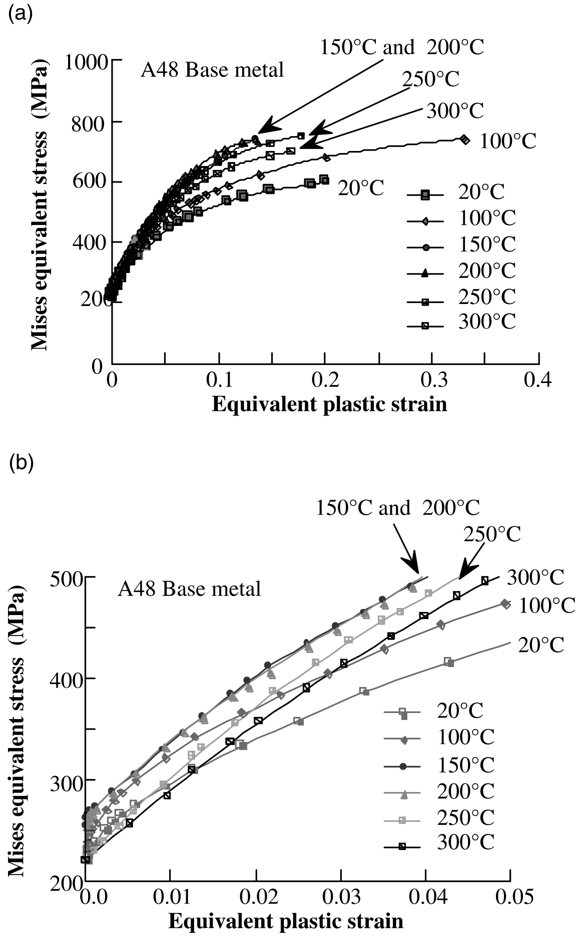

Fig. 11. Von Mises equivalent stress–strain curves used for numerical analysis. (a) Whole curves; (b) detail of the curves at low strains.

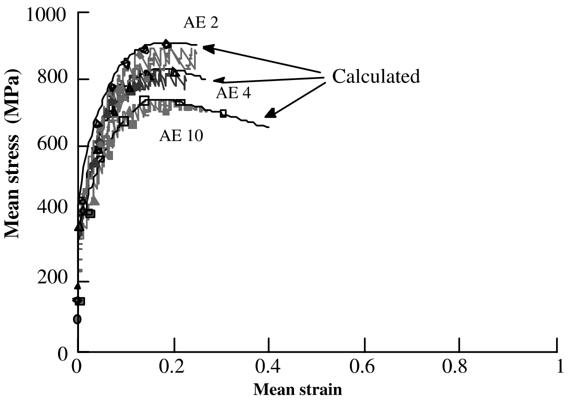

Fig. 12. Comparison of the calculated and experimental mean stress–mean strain curves for base metal at $T = 150$ °C.

4.2. Cavity growth modelling

The critical value of void growth $(R/R_0)_c$ can then be calculated (for each geometry of the axisymmetric notched specimens and each temperature) by integrating the Rice and Tracey expression between ε_d and ε_R. The strain necessary to nucleate cavities from inclusions ε_d is assumed to be so small that this value is set to zero. The strain at failure ε_R is taken from the tensile tests on the axisymmetric notched specimens. For each temperature, the mean critical value of $\ln(R/R_0)_c$ is calculated (Fig. 13 for base metal at 100 °C for example) for the different stress triaxiality ratios for the different geometries of axisymmetric notched specimens. The variation of the mean critical void growth parameter, $\ln(R/R_0)_c$, versus temperature is plotted for the A48 base and weld deposited metals in Figs. 14 and 15. The scatter due to different stress triaxiality ratios is indicated on these

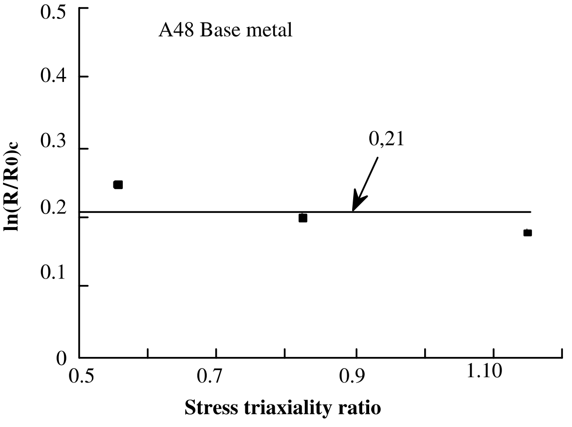

Fig. 13. Mean critical value of $\ln(R/R_0)_c$ for different stress triaxiality ratios (at $T = 100$ °C).

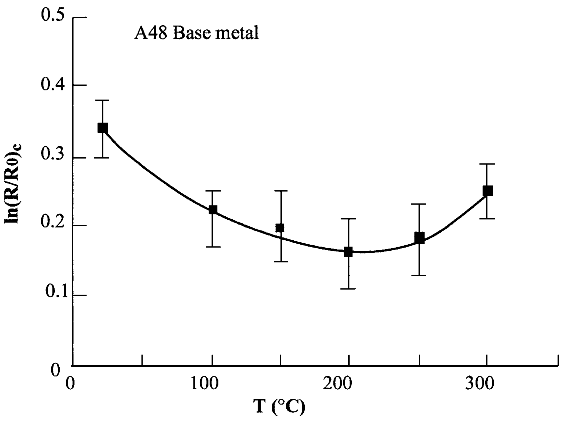

Fig. 14. Variation of mean critical void growth parameter, $\ln(R/R_0)_c$, versus temperature for base metal.

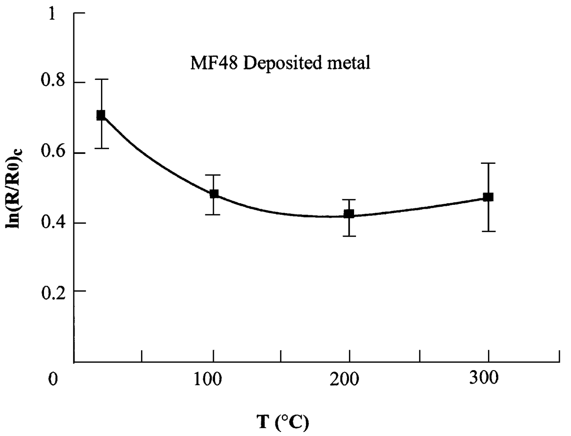

Fig. 15. Variation of mean critical void growth parameter, $\ln(R/R_0)_c$, versus temperature for weld deposited metal.

figures. Even taking into account this scatter, these figures show clearly a minimum in the critical void growth parameter for a temperature close to 200 °C, in agreement with the observed temperature minima for $J_{0.2}$ and $\mathrm{d}J/\mathrm{d}a$.

4.3. J modelling

The strain field ε_{ij} at the crack tip can be described by the Hutchinson–Rice–Rosengren solution. Relationship can then be established between $J_{0.2}$ (and $\mathrm{d}J/\mathrm{d}a$), the yield stress of the material, σ_y, and the critical void growth parameter, $(R/R_0)_c$, as follows:

$$J_{0.2} = \alpha\sigma_y(\Delta a)_c \ln(R/R_0)_c, \tag{5}$$

$$\mathrm{d}J/\mathrm{d}a = \beta\sigma_y(\Delta a)_c \ln(R/R_0)_c. \tag{6}$$

In this expression, α and β correspond to numerical constants ($\alpha \approx 4.5$ for CT specimens), whereas $(\Delta a)_c$ represents a characteristic distance of the microstructure (according to the strain rate is the same order in CTJ and axisymmetric specimens).

In this study, the product $\alpha(\Delta a)_c$ was chosen so as to obtain the best fit between the model and the experimental results for $J_{0.2}$ (or $\beta(\Delta a)_c$ for $\mathrm{d}J/\mathrm{d}a$). For the A48 base metal, the comparison between calculated and experimental values is given versus temperature in Fig. 16 for $J_{0.2}$ and in Fig. 17 for $\mathrm{d}J/\mathrm{d}a$. For the crack initiation resistance $J_{0.2}$, $\alpha(\Delta a)_c$ was found to be equal to 1.4 mm. With α taken as 4.5, we obtained $(\Delta a)_c$ equal to about 0.310 mm. For $\mathrm{d}J/\mathrm{d}a$ (Fig. 17), $\beta(\Delta a)_c$ was found to be about 1.67. Thus, with a value of $(\Delta a)_c = 0.310$ mm, we obtained $\beta = 5.4$.

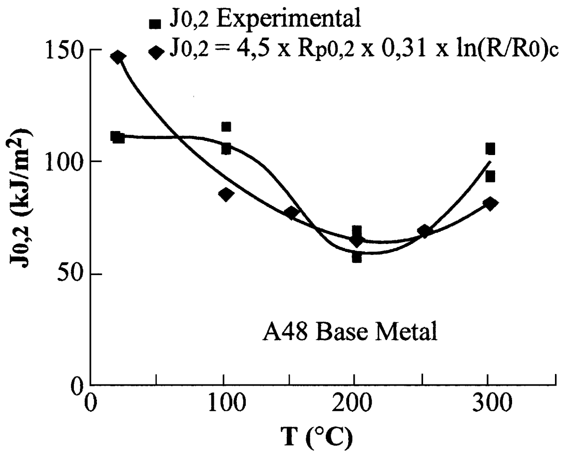

Fig. 16. Comparison of calculated and experimental $J_{0.2}$ values for base metal.

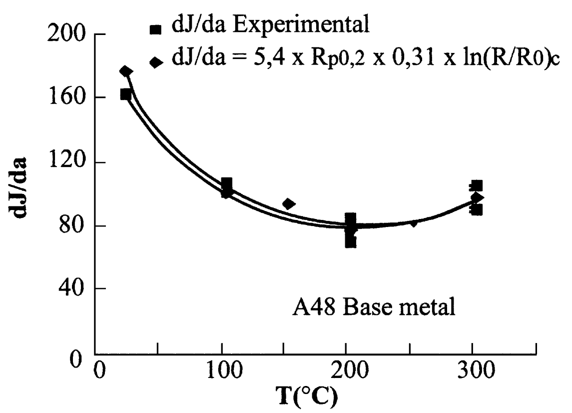

Fig. 17. Comparison of the calculated–experimental $\mathrm{d}J/\mathrm{d}a$ values for base metal.

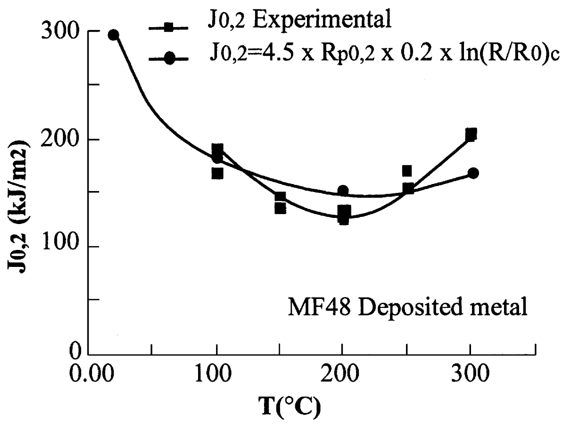

Fig. 18. Comparison of calculated and experimental $J_{0.2}$ values for weld deposited metal.

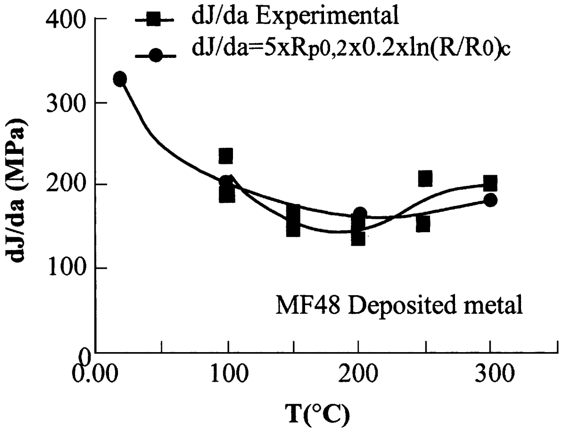

Fig. 19. Comparison of calculated and experimental dJ/da values for weld deposited metal.

For the weld deposited metal (Figs. 18 and 19), the fit between the calculated and experimental $J_{0.2}$ values gives $(\Delta a)_c = 0.200$ mm for the characteristic distance. For the tearing modulus dJ/da, $\beta(\Delta a)_c \approx 1.00$. Hence, with $(\Delta a)_c$ of 0.2 mm, we obtained $\beta = 5$. These characteristic parameters are related to the microstructure in the discussion.

5. Discussion

For the commercial C–Mn steels (base metals and associated welds) studied here that were sensitive to DSA phenomenon, the variation of fracture toughness versus temperature reveals a maximum ductility loss at a temperature close to 200 °C. The higher sensitivity to DSA, the larger is the decrease in ductility observed. The increase of the work hardening rate n, which is observed when DSA is present, causes an increase in the flow stress and in the crack tip plastic radius r_p (which is proportional to n^2), thus decreasing the void growth rate. An increase in the fracture toughness is consequently expected in the DSA temperature range. This is in fact observed in a Armco pure iron, as reported by Srinivas et al. [23,24] and Hong and Linga Murty [25]. In pure iron, these authors have observed an increase in fracture toughness from room temperature to 200 °C and then a decrease. By contrast, these pure irons showed the same DSA effect as other DSA sensitive materials for tensile properties such as the maximum in UTS and work hardening rate, the minimum in elongation and reduction of area. For these authors, this difference in behaviour compared to commercial steels is attributed to the absence of inclusions in pure iron, which modifies the ductile damage process. In pure iron, the nucleation of microvoids is due to dislocation pile ups on grain boundaries or intersecting slip bands that requires high plastic strains. In commercial steels, on the other hand, the damage process is governed by cavity nucleation and growth from inclusions. The model used in this study, based on the growth of cavities nucleated from inclusions, predicts correctly the decrease of fracture toughness and justifies this assumption.

For the A48 *base metal*, an in situ tensile test was carried out at 20 °C in a scanning electron microscope to follow the evolution of the damage process. The specimen direction was transverse to the rolling direction and the observed surface was in the transverse–longitudinal plane. The test was interrupted at different strains to allow observations. The recorded stress–strain curve is given in Fig. 20.

Nine observations were conducted at different strain amplitudes. At the beginning (step 0), clusters of large elongated inclusions in the longitudinal direction (Fig. 21(a)) were visible in the middle of the sample. They were mixed inclusions (silicon and aluminium oxides

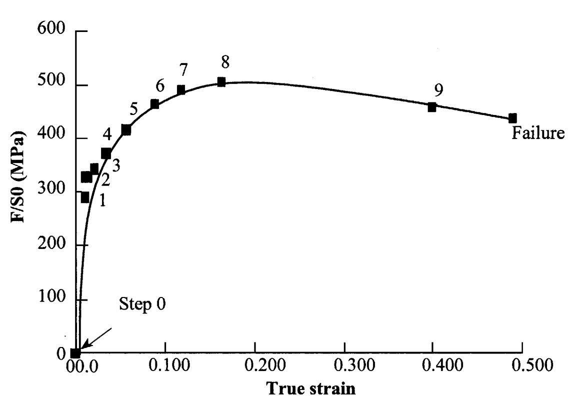

Fig. 20. Conventional stress–true strain curve recorded during the in situ tensile test.

(Al_2O_3, SiO_2, CaO) with manganese sulphide (MnS)), and failure occurred mainly at these inclusions. The other inclusions observed were globular manganese sulphides. Stage I of the damage process occurred very early (from step 2 for some inclusions) by nucleation of microvoids between manganese sulphides and the matrix (Fig. 21(b)). At step 6 (10% strain), all inclusions showed at least one microvoid. After this nucleation stage, microvoid growth was observed (Fig. 21(c) and (d)), and, at this same inclusion, cleavage occurred in the oxide or sulphide (Fig. 21(d)). For high strains, large inclusions were fracture in small pieces, and cavity growth

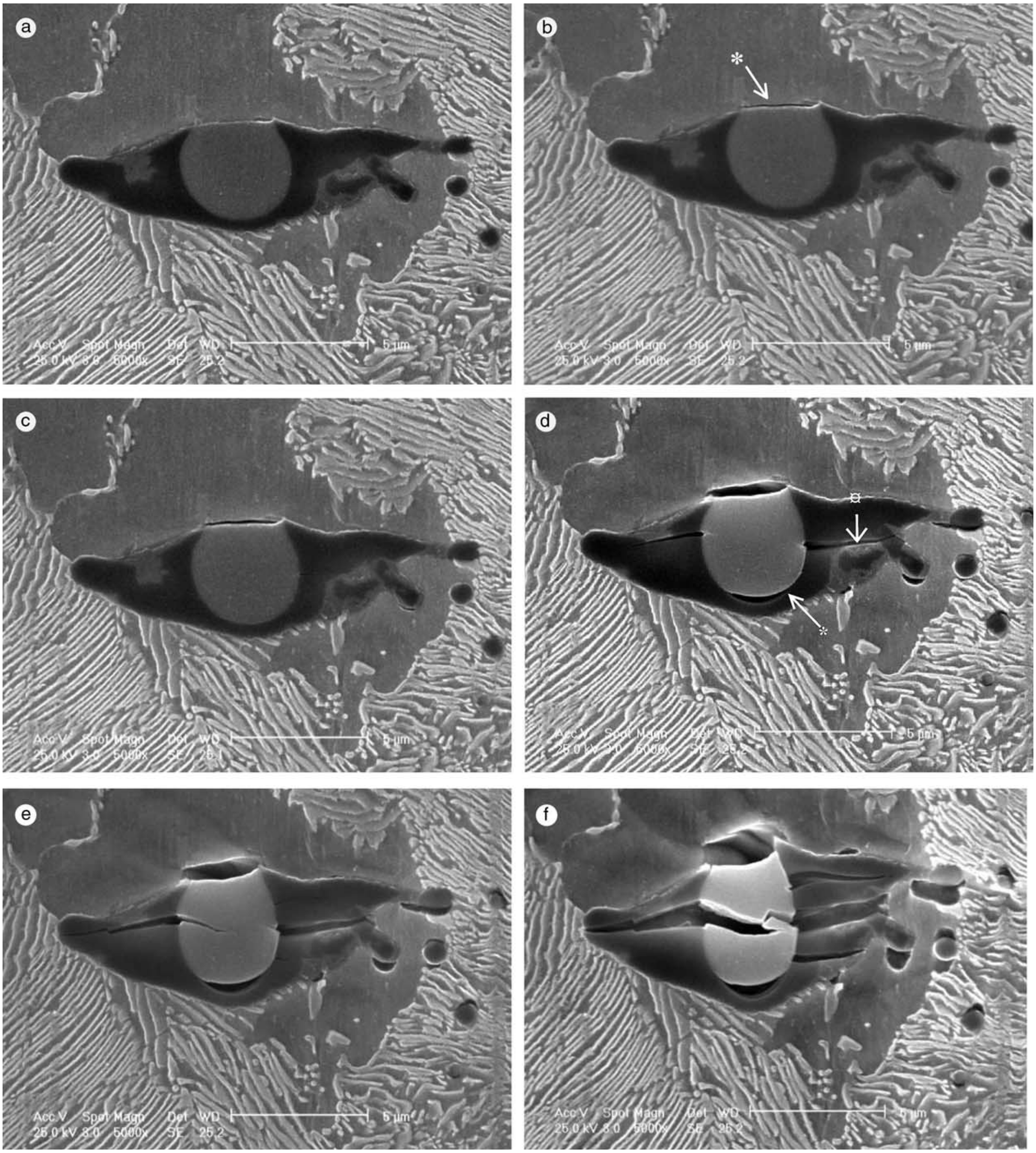

Fig. 21. In situ tensile test: nucleation and failure of mixed inclusions.

progressed to failure. From step 4 (5% strain), some slip bands appeared in the ferrite. When the slip direction was nearly perpendicular to the plane of cementite lamella, slip produced failure of these lamella (Fig. 22(a) and (b)). When the slip direction was nearly parallel to the cementite lamella, no failure was observed in the pearlite. Thus, some slip bands can induce failure by shearing of pearlite grains, and the nucleated cavities grow in the same way as the cavities initiating from inclusions (Fig. 22(c) and (d)). On the fracture surface, we observed three kinds of dimples: elongated dimples nucleated from mixed inclusions (Fig. 22(e)), small dimples nucleated from manganese sulphides inclusions and dimples nucleated by the growth of the sheared pearlite grains (Fig. 22(f)).

Scanning electron microscope examinations of the fracture surface of the axisymmetric notched specimens showed the same kinds of dimples (Fig. 23). Whatever the temperature (in the DSA temperature range or outside), three kinds of dimples were observed and the size

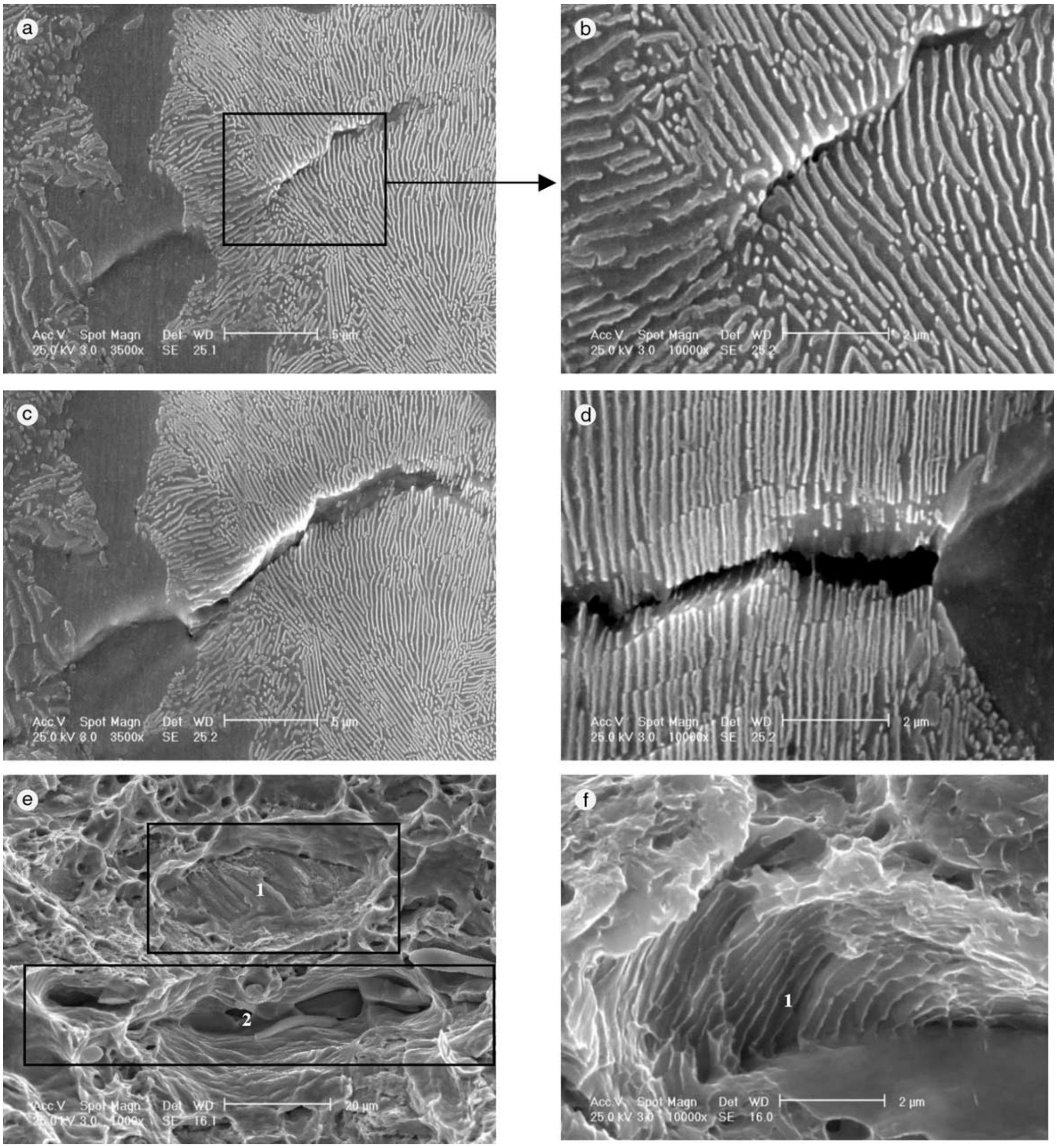

Fig. 22. In situ tensile test: fracture in pearlite grain.

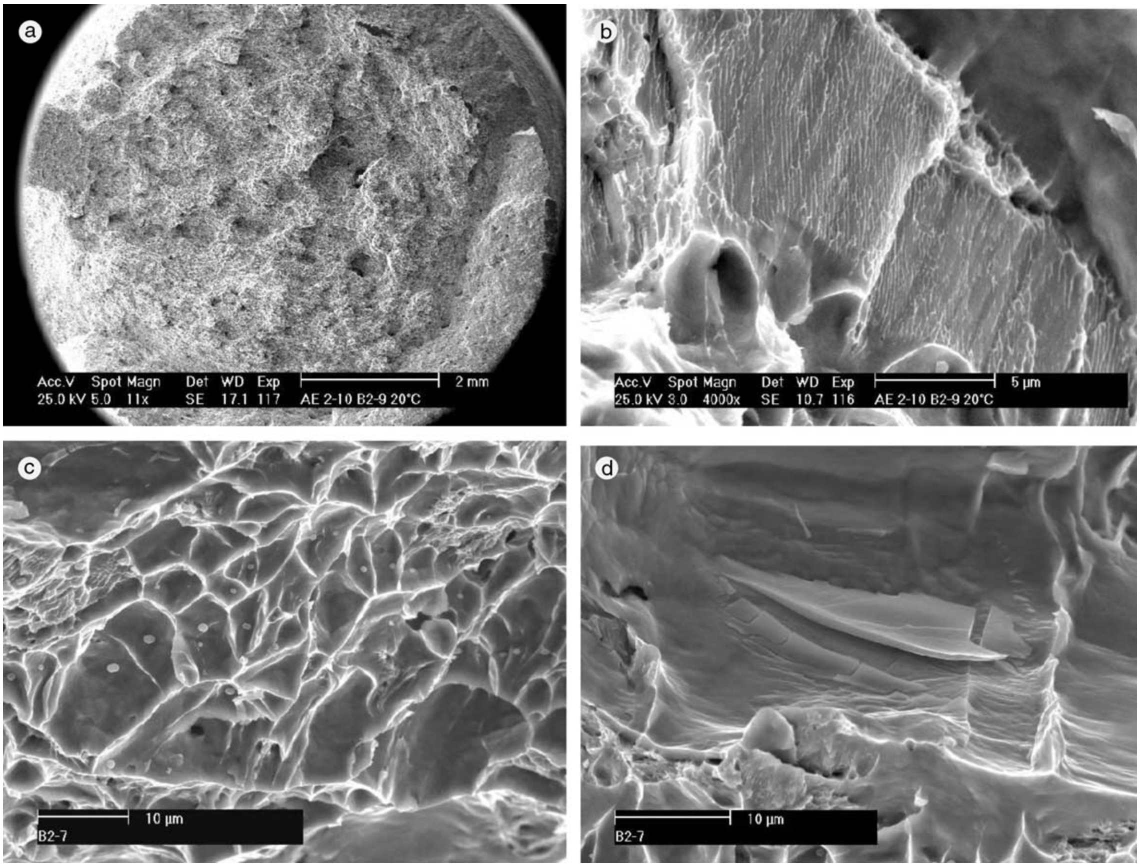

Fig. 23. Fractographic examinations of axisymmetric notched specimens for base metal.

of these dimples did not vary with the test temperature. This means, that the mechanism of failure was the same whether DSA was present or not.

For the base metal, the mean distance between inclusions was about 0.065 mm in the STL plane, and the mean distance between the pearlite bands about 0.040 mm. Therefore, the characteristic distance $(\Delta a)_c$ of 0.310 mm (deduced from the fit between calculated and experimental $J_{0.2}$ values) seems to be related to the mean distance between inclusion clusters, which create the macrocavities observed on the fracture surface of the axisymmetic notched specimens. This is in good agrement with the microstructure analysis made by Beauvineau [39] on a C–Mn steel (with a higher volume fraction of inclusions than the steel in this study). He found a mean distance between inclusions of 0.040 mm and a mean distance between inclusion clusters of 0.300 mm.

For the *deposited metal*, only fractographic examinations of axisymmetric notched specimens were made. Macrographic examinations showed secondary cracks (Fig. 24(b)) and concentric 'ridges' (Fig. 24(a)). Perpendicular polished sections of the specimens have shown that these ridges do not seem to be related to the different runs of the weld. Houssin et al. [40] reported the same feature on a weld of a low alloy steel (SA 508Cl3). In this case, the 'ridges' seemed to be related to the proeutectoid ferrite of the non-recrystallized zone of the layer. More observations are needed to clarify this point. For the weld deposited metal studied, here, SEM micrographic examinations showed only one kind of dimple (independent of temperature) nucleated from oxide inclusions (Fig. 24(c)). The mean distance between these inclusions was about 0.0055 mm. Thus, the characteristic distance $(\Delta a)_c$ (0.200 mm) found for this microstructure is larger than the mean distance between inclusions. $(\Delta a)_c$ is closer to the distance between the peaks and the hollows of the 'ridges' observed on the fracture surface of the axisymmetric notched specimens.

In both materials, independent of temperature in or out of the DSA temperature range, the main features of the ductile dimples were the same. Thus, the DSA phenomenon seemed to affect only the occurrence of the different stages of ductile fracture. According to Srinivas et al. [23–25], the increase in work hardening rate enables the stress for nucleation of microvoids (stage I) to be reached at lower strains, which explains the decrease

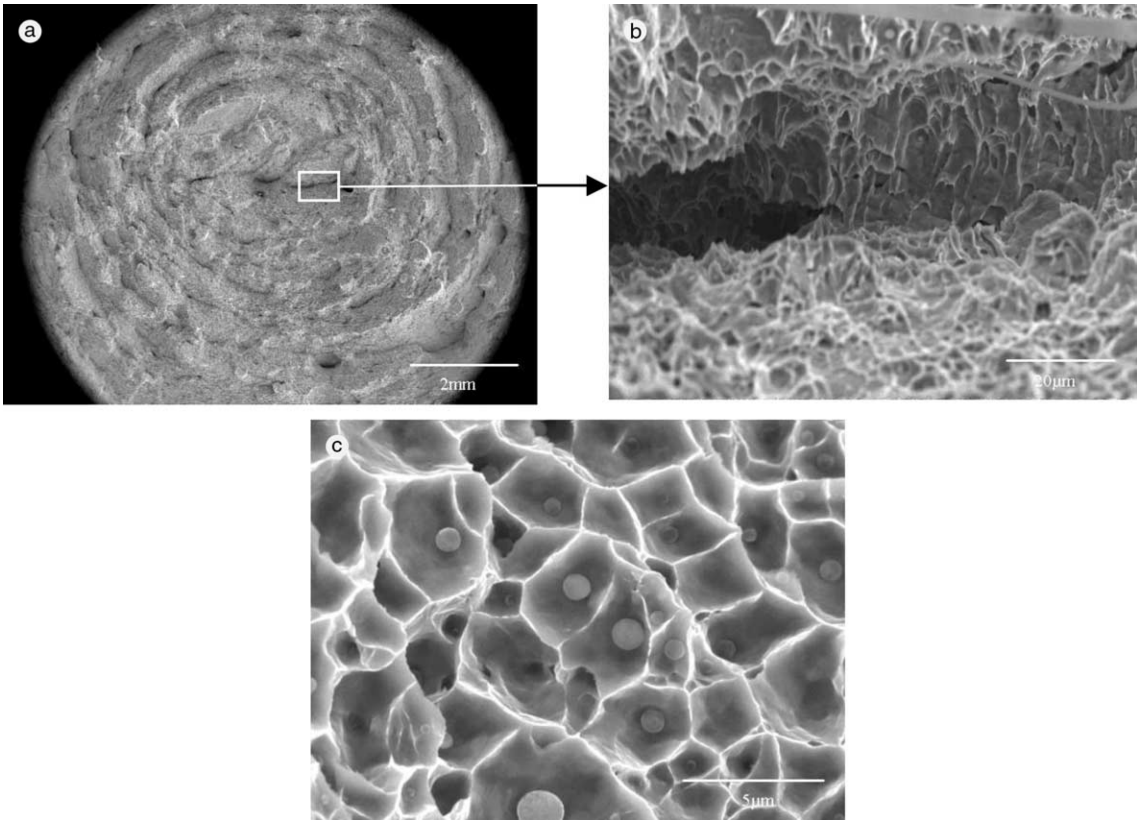

Fig. 24. Fractographic examinations of axisymmetric notched specimens for weld deposited metal.

in elongation and fracture toughness. In our modelling, the strain necessary to nucleate cavities from inclusions ε_d was assumed to be zero and so, no resolution of this question can be deduced from our model. However, an another interpretation can be proposed. The occurrence of DSA is always associated with a minimum in elongation due to the decrease of the strain rate sensitivity coefficient $S = \mathrm{d}\sigma/\mathrm{d}\log\varepsilon$. If the strain rate sensitivity coefficient is high, the increase in local strain rate in the necking area induces a large increase in the flow stress. This is contrary to the plasticity confinement hypothesis. Consequently, plastic strain tends to become homogeneous. On the other hand, a decrease in strain rate sensitivity favours plasticity confinement and premature failure. Thus, in the DSA temperature range, the third stage probably occurs earlier, inducing a decrease of $J_{0.2}$ and $\mathrm{d}J/\mathrm{d}a$.

Since, the model used (integrated between zero and the failure strain ε_R) correctly predicts the decrease of $J_{0.2}$ and $\mathrm{d}J/\mathrm{d}a$, and since the evolution of strain at failure ε_R is similar to that of the uniform strain $\varepsilon_{\mathrm{uniform}}$ (the strain at the onset of stage III in the ductile failure process), it is predicted that the early occurrence of stage III is the main consequence of the DSA effect.

For better insight into the influence of DSA on ductility, it would be necessary to evaluate by optical micrographic examinations the nucleation strain ε_d in order to integrate the model between ε_d and $\varepsilon_{\mathrm{uniform}}$. In other respects, the present model is an uncoupled model, and it would be better to use a coupled model (Gurson's model for example). Nevertheless, in this case, the main difficulty is to take into account the true experimental stress–strain curve for modelling the stress–strain field at the crack tip, since negative strain rate sensitivity induces unstable numerical calculations.

6. Conclusion

In commercial C–Mn steels sensitive to DSA (base metals and associated welds), the variation of fracture toughness versus temperature reveals a ductility loss located at about 200 °C. The higher the sensitivity to DSA, the larger the decrease in ductility.

Fractographic examinations have shown that the failure mechanism itself is not affected by the DSA phenomenon (e.g. same size of ductile dimples whatever the temperature). DSA seems to modify the final stage of ductile tearing resulting from shear localization between voids.

A model of this ductility decrease has been proposed using the local approach to ductile fracture. The damage model used was the Rice and Tracey cavity growth model, integrated between zero and the strain to failure. The associated decreases of $J_{0.2}$ and dJ/da are correctly predicted. Further developments are required to explain the difference between pure iron and commercial steels.

Acknowledgements

The authors want to gratefully acknowledge the contribution of Dr P. Scott for reviewing the manuscript and making useful comments.

References

[1] J.D. Baird, Iron Steels (1963) 186, 326, 368, 400, 450.
[2] J.D. Baird, Met. Rev. 149 (1971) 1.
[3] J.D. Baird, The Inhomogeneity of Plastic Deformation, ASM, Metals Park, OH, 1973 (p. 191).
[4] A.S. Keh, Y. Nakada, W.C. Leslie, Dislocation Dynamics, McGraw-Hill, New York, 1968 (p. 381).
[5] W.C. Leslie, in: Encyclopedia of Materials Science and Engineering, vol. 5, Pergamon, Oxford, 1986 (p. 4007).
[6] P. Lacombe, Matér. Techn. (1985) E5–E15.
[7] A.H. Cottrell, Crystals, Clarendon, Oxford, 1953.
[8] P.G. Mccormick, Acta Metall. 20 (1972) 35.
[9] A. van den Buekel, Phys. Stat. Sol. 30 (1975) 197.
[10] A.W. Sleeswijk, Acta Metall. 6 (1958) 598.
[11] R.A. Mulford, U.F. Kocks, Acta Metall. 27 (1979) 1125.
[12] L.P. Kubin, Y. Estrin, J. Phys. III 1 (1991) 929.
[13] C.W. Marschall, M.P. Landow, G.M. Wilkowski, ASTM STP 1074 (1990) 339.
[14] D. Wagner, J.C. Moreno, C. Prioul, J.M. Frund, B. Houssin, Rev. Met.-CIT/SGM 5 (2001) 473.
[15] J.M. Frund, B. Marini, M. Bethmont, Etude de la résistance à la déchirure ductile des structures: influence des dimensions et de la géométrie des éprouvettes sur l'amorçage et la propagation de la déchirure ductile, Séminaire EDF 'Mécanique des structures', Beaune, 11–13 mai 1993.
[16] M.T. Miglin, W.A. van der Sluys, R.J. Futato, H.A. Domian, ASTM STP 856 (1985) 150.
[17] R. Moskovic, Eng. Fract. Mech. 30 (6) 839.
[18] J.H. Yoon, B.S. Lee, Y.J. Oh, J.H. Hong, Int. J. Pres. Ves. Pip. 76 (1999) 663.
[19] N. Bailey, J.R. Gordon, N.V. Challenger, H.G. Pisarski, Strain ageing embrittlement of repair weld metals for service up to 350 °C, Final report, Welding Institute 5555/40A/91, 1991.
[20] J.G. Feldstein, Repair welding of heavy section steel components in LWRs, E.P.R.I. Report NP-3614,1, Palo Alto, CA, 1984.
[21] P. Soulat, B. Houssin, An. Mecan. Fract. 9 (1992) 226.
[22] I.S. Kim, S. Kang, Int. J. Pres. Ves. Pip. 62 (1995) 123.
[23] M. Srinivas, G. Malakondaiah, K. Linga Murty, P.R. Rao, Scripta Met. Mater. 25 (1991) 2585.
[24] M. Srinivas, G. Malakondaiah, P.R. Rao, Acta Metall. Mater. 41 (4) (1993) 1301.
[25] J.H. Hong, K. Linga Murty, in: P.K. Liaw, R. Viswanathan, K.L. Murty, E.P. Simonen, D. Frear (Eds.), First International Conference on Microstructures and Mechanical Properties of Ageing Materials, Chicago, USA, November 1992, The Minerals, Metals and Materials Society, 1993, p. 391.
[26] P.F. Thomason, Fat. Fract. Eng. Mater. Struct. 21 (1998) 1105.
[27] G. Sanz, B. Marandet, Application des concepts mécaniques de la rupture à l'étude d'aciers de construction, Rapport CECA 7210, 1983.
[28] B.H. Menke, A.L. Hiser, J.R. Hawthorne, F.J. Loss, R curve characterisation of low strength structural steels, EPRI Report 2715, 1982.
[29] A.D. Wilson, J. Eng. Mater. Technol. 101 (1979) 265.
[30] A.D. Wilson, ASTM STP 668 (1979) 469.
[31] R. Roberts, G.V. Krishna, J. Nishanian, ASTM STP 700 (1980) 552.
[32] R. Roberts, C. Newton, Interpretive report on small scale tests correlations with K_{Ic} data, WRC Bulletin 205 (1989).
[33] D. Wagner, J.C. Moreno, C. Prioul, Rev. Met.-CIT/SGM 12 (2000) 1481.
[34] J.R. Rice, D.M. Tracey, J. Mech. Phys. Sol. 17 (1969) 201.
[35] A.G. Franklin, J. Iron Steel Inst. (1969) 181.
[36] N. Bailey, N.V. Challeneger, Survey of parameters governing ductile tearing behaviour of C–Mn steel, Welding Institute Report 28821/1/90, 1990.
[37] Groupe Fragilité rupture, Recommandation d'essais de mesure de la résistance à la déchirure ductile des matériaux métalliques, Procédure GFR, 1990.
[38] F.M. Beremin, J. Méc. Appl. 4 (3) (1980) 327.
[39] L. Beauvineau, Approche locale de la rupture ductile: application à un acier au C–Mn, Thèse ENSMP, 1996.
[40] B. Houssin, J.P. Chavaillard, C. Coudert, Nucl. Eng. Des. 87 (1985) 73.